




Coupling of microwave photons to optical and acoustic magnon modes in the layered antiferromagnetic insulator CrCl_3

Qi Zhang, Jianshu Xue, Yitong Sun, Jiajun Guo, Yanxue Chen, Yufeng Tian , Shishen Yan, and Lihui Bai ^{*}
School of Physics, State Key Laboratory of Crystal Materials, Shandong University, Jinan 250100, China

 (Received 31 May 2021; revised 9 August 2021; accepted 24 August 2021; published 7 September 2021)

We study a magnon-photon coupling system consisting of a layered antiferromagnetic insulator CrCl_3 and a planar superconducting cavity. By changing the position of the CrCl_3 crystal on the cavity, we separately demonstrate the cavity mode coupled with an acoustic mode and an optical mode when the magnetic moments are in a spin-flop transition. Based on the coupled Landau-Lifshitz-Gilbert equations and Kirchhoff's equation, we predict that both the net magnetization and the Néel vector contribute to the coupling between the optical mode and cavity mode, and only the net magnetization participates in the coupling of the acoustic mode and cavity mode. This paper highlights the vital role played by the Néel vector as the key parameter of an antiferromagnet in magnon-photon coupling, which offers insight into designing antiferromagnet spintronic devices.

DOI: [10.1103/PhysRevB.104.094303](https://doi.org/10.1103/PhysRevB.104.094303)

I. INTRODUCTION

Magnon and photon coupling systems have many potential applications in quantum information processing because the information can be coherently transformed from magnons to photons when they are strongly coupling together via a dipolar interaction [1–4]. By placing a magnetic element in a microwave cavity, magnon-photon coupling has been extensively studied and reported [5–13], in which research mostly focused on ferromagnetic materials, such as insulator yttrium iron garnet (YIG) and permalloy (Py) [14–17]. Different from the ferromagnetic material, an antiferromagnet has a high spin dynamics frequency from subterahertz to terahertz (THz) and no net magnetization due to the compensated magnetization from each sublattice [18–23]. Therefore, the spintronic devices based on antiferromagnets have a higher speed and better stability. Usually, the excitation of antiferromagnetic resonance prefers a high magnetic field to compete with the strong exchange interaction in the antiferromagnets, and the high dynamic frequency makes the measurement require THz technology. Furthermore, the magnon-photon coupling in antiferromagnets is predicted to be much weaker than in ferromagnets due to the absence of net magnetization [24,25]. Therefore, the coupling between the photons and the magnons in an antiferromagnet is not well understood. Few experimental studies have been reported on the magnon-photon coupling in antiferromagnets, including di(phenyl)-(2,4,6-trinitrophenyl)iminoazanium (DPPH), dysprosium ferrite (DyFeO_3), and GdVO_4 [26–28]. However, these reports so far have mostly focused on the coupling of photons and magnons in antiferromagnets with collinear magnetization.

CrCl_3 is a layered antiferromagnetic insulator below a Néel temperature of 14 K [29,30]. Because of weak interlayer

coupling, the antiferromagnetic resonance in CrCl_3 can be explored in a low frequency of GHz. The in-plane anisotropy field is relatively weak and ignorable. By applying a static magnetic field H , the antiparallel net magnetizations in two magnetic sublattices are no longer collinear and turn to the direction of H , which is known as a spin-flop transition. The angle between the net magnetization is inversely proportional to the applied magnetic field [31]. The layered CrCl_3 provides a platform for studying the coupling between the microwave photons and the magnons in an antiferromagnet when the magnetizations are in a spin-flop transition.

In this paper, using CrCl_3 and a superconducting cavity, we study the coupling of the microwave photons and the antiferromagnetic magnons in a spin-flop transition. We demonstrate the acoustic mode and the optical mode of the antiferromagnetic resonances can be separately excited when the microwave magnetic field and external magnetic field satisfy certain symmetry rules. Both optical and acoustic branches show dispersion anticrossing features when the magnon modes cross the cavity modes, and the coupling strength for the optical mode is larger than that for the acoustic mode. Furthermore, we predict that both the net magnetization \mathbf{M} and the Néel vector \mathbf{N} take part in the coupling of the optical mode and cavity mode, and only the net magnetization works in the acoustic mode and cavity mode coupling system, which has the same physics as the coupling of ferromagnetic materials and cavities. Our results experientially and theoretically reveal the mechanism of the coupling between the antiferromagnetic magnons and the microwave photons.

II. EXPERIMENTAL METHODS

The platelike CrCl_3 single crystals used in this study are grown by anhydrous CrCl_3 powder using chemical vapor transport [29]. The synthesized CrCl_3 crystals are shown in the inset of Fig. 1(a). The x-ray diffraction data in Fig. 1(a) can be indexed by the $(00l)$ plane which indicates the surface

^{*}lhbai@sdu.edu.cn

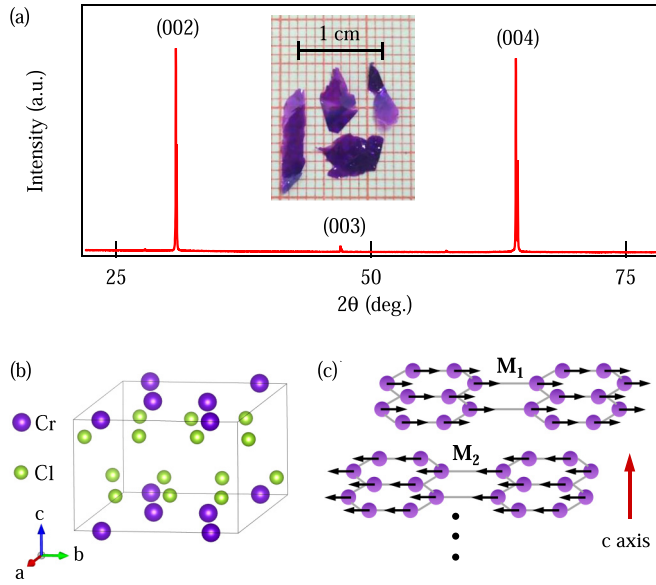


FIG. 1. (a) X-ray diffraction pattern from the plane of a CrCl_3 crystal. The platelike CrCl_3 single crystals grown by chemical vapor transport are shown in the inset. (b) Crystal structure of CrCl_3 . (c) Magnetic structure of CrCl_3 at zero magnetic field while below the Néel temperature.

of the crystal is parallel to the plane of a and b . CrCl_3 is monoclinic with a layered structure, and the crystal structure with an interlayer spacing of 5.798 \AA is shown in Fig. 1(b), where the purple and green spheres represent the Cr and Cl atoms, respectively. The magnetic structure of two adjacent layers without an external magnetic field is shown in Fig. 1(c). CrCl_3 is an antiferromagnet with two magnetic sublattices (M_1 and M_2) below the Néel temperature. The magnetic moments are parallel in the same layer and antiparallel between two adjacent layers [30].

A superconducting cavity is fabricated by photolithography and reactive ion etching techniques using a $650\text{-}\mu\text{m}$ -thick DyBaCuO film deposited on a 0.5-mm -thick MgO substrate. As shown in Fig. 2(a), the microstrip cavity has a length of 7.8 mm and a width of 0.48 mm . Capacitive coupling between the planar cavity and the signal lines is realized by a 0.5-mm gap in between. A vector network analyzer (VNA) with an excitation power of 5 dBm was used to measure the microwave transmission spectrum $|S_{21}|$ at 4 K which is well below the superconducting transition temperature of 89 K for DyBaCuO and the Néel temperature of 14 K for CrCl_3 . The Cartesian coordinate is established with the x and y axis in the plane and the z axis out of plane. The external static magnetic field H is applied along the y axis in the experiment. The measured transmission spectra of the superconducting cavity without a sample are shown in Fig. 2(b). This cavity exhibits a sharp resonance peak at $\omega_c/2\pi = 7.349 \text{ GHz}$ and an intrinsic loss rate $\beta = \delta\omega/\omega_c = 8.1 \times 10^{-5}$ which is determined by the half width at half maximum $\delta\omega/2\pi = 595 \text{ kHz}$. By sweeping $\mu_0 H$ from 0 to 0.8 T , the rate of change for the resonant frequency of the cavity is less than 0.04% , as shown in Fig. 2(c). This indicates that the cavity exhibits excellent stability, and the influence of magnetic flux vortices in the superconducting

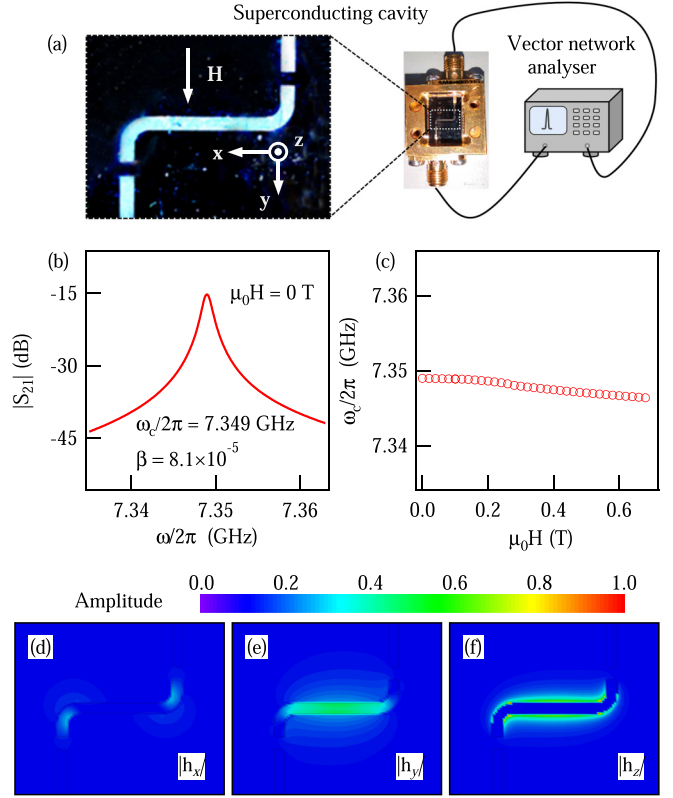


FIG. 2. (a) A schematic diagram for the experimental setup. The amplified portion shows the structure of the superconducting cavity. (b) The transmission spectra $|S_{21}|$ of the typical cavity mode without the sample. (c) The resonance frequency shifts with the external magnetic fields. The microwave magnetic field distributions of (d) $|h_x|$, (e) $|h_y|$, and (f) $|h_z|$ on the surface of a superconducting cavity.

cavity can be ignored [32]. To clarify the characteristics of the microwave magnetic field \mathbf{h} , the simulated amplitude distributions of the in-plane components (h_x and h_y) and out-of-plane component (h_z) at the resonance frequency of the cavity are shown in Figs. 2(d)–2(f), respectively. The amplitude of h_x almost vanishes near the horizontal part of the cavity. The component of h_y concentrates on the top of the cavity, and h_z distributes on both sides of the cavity.

III. COUPLING MODEL

The coupling between the cavity and antiferromagnetic resonance modes includes two basic physical systems. One is the magnetization dynamics system which possesses two magnetic sublattices and the other is a superconducting microwave cavity with a low intrinsic loss rate and high stability. The dynamics of \mathbf{M}_1 and \mathbf{M}_2 in CrCl_3 can be described by two coupled Landau-Lifshitz-Gilbert (LLG) equations [30],

$$\frac{d\mathbf{M}_1}{dt} = -\mu_0\gamma\mathbf{M}_1 \times \mathbf{H}_{\text{eff}1} + \frac{\alpha}{M_s}\mathbf{M}_1 \times \frac{d\mathbf{M}_1}{dt}, \quad (1a)$$

$$\frac{d\mathbf{M}_2}{dt} = -\mu_0\gamma\mathbf{M}_2 \times \mathbf{H}_{\text{eff}2} + \frac{\alpha}{M_s}\mathbf{M}_2 \times \frac{d\mathbf{M}_2}{dt}, \quad (1b)$$

where μ_0 and γ are the permeability of the vacuum and the gyromagnetic ratio, respectively. $\alpha = 0.032$ is the intrinsic

Gilbert damping of CrCl₃. When the external magnetic field \mathbf{H} is applied along the y axis, the effective magnetic field is $\mathbf{H}_{\text{eff}1(2)} = \mathbf{H}_y + \mathbf{h} - (H_E/M_s)\mathbf{M}_{2(1)} - (\mathbf{M}_{1(2)} \cdot \hat{z})\hat{z}$, where H_E and M_s are the interlayer exchange field and the saturation magnetization, respectively. We define $\mathbf{M}_{1(2)} = \mathbf{M}_{1(2)}^{\text{eq}} + \mathbf{m}_{1(2)}e^{i\omega t}$ with $\mathbf{M}_{1(2)}^{\text{eq}}$ being the magnetization in the equilibrium position. Using the relations of $\mathbf{m}_a = \mathbf{m}_1 - C_{2y}\mathbf{m}_2$ and $\mathbf{m}_o = \mathbf{m}_1 + C_{2y}\mathbf{m}_2$, where C_{2y} is defined to describe the 180° rotation around the y axis, the LLG equations can be decoupled as

$$i\omega\mathbf{m}_a = \mu_0\gamma\mathbf{M}_1^{\text{eq}} \times \mathbf{H}_{\text{eff}a} + \frac{i\alpha\omega}{M_s}\mathbf{M}_1^{\text{eq}} \times \mathbf{m}_a, \quad (2a)$$

$$i\omega\mathbf{m}_o = \mu_0\gamma\mathbf{M}_1^{\text{eq}} \times \mathbf{H}_{\text{eff}o} + \frac{i\alpha\omega}{M_s}\mathbf{M}_1^{\text{eq}} \times \mathbf{m}_o, \quad (2b)$$

where $\mathbf{H}_{\text{eff}a} = (H_E/M_s)(\mathbf{m}_a - C_{2y}\mathbf{m}_o) + (\mathbf{m}_a \cdot \hat{z})\hat{z} - \mathbf{h}_a$ and $\mathbf{H}_{\text{eff}o} = (H_E/M_s)(\mathbf{m}_o + C_{2y}\mathbf{m}_a) + (\mathbf{m}_o \cdot \hat{z})\hat{z} - \mathbf{h}_o$. We establish a new coordinate (m_ϕ, m_θ) to simply solve Eq. (2), where m_ϕ and m_θ are perpendicular and parallel to the sample plane, respectively, as shown in Fig. 3(a). The linear solutions of Eq. (2) in a small-angle approximation for the acoustic mode and optical mode are

$$\begin{pmatrix} m_{a\phi} \\ m_{a\theta} \end{pmatrix} = \frac{-2\omega_m}{\omega^2 - \omega_{ra}^2 - i\alpha\omega\omega_{pa}} \begin{pmatrix} i\omega \\ 2\omega_e \sin^2 \phi + i\alpha\omega \end{pmatrix} h_\theta, \quad (3a)$$

$$\begin{pmatrix} m_{o\phi} \\ m_{o\theta} \end{pmatrix} = \frac{-2\omega_m \cos^2 \phi}{\omega^2 - \omega_{ro}^2 - i\alpha\omega\omega_{po}} \begin{pmatrix} \omega_m + i\alpha\omega \\ -i\omega \end{pmatrix} h_\phi. \quad (3b)$$

where $\sin \phi = H/(2H_E)$, $\omega_e = \mu_0\gamma H_E$, $\omega_m = \mu_0\gamma M_s$, $\omega_{pa} = 2\omega_e(1 + \sin^2 \phi) + \omega_m$, and $\omega_{po} = 2\omega_e \cos^2 \phi + \omega_m$. The resonant frequencies for the acoustic mode ω_{ra} and optical mode ω_{ro} have a magnetic field dependence of $\omega_{ra} = \sqrt{2\omega_e(2\omega_e + \omega_m)} \sin \phi$ and $\omega_{ro} = \sqrt{2\omega_e\omega_m} \cos \phi$. According to the measured dispersion of the acoustic mode and optical mode (see the Appendix), we obtain the fitting parameters $\mu_0 H_E = 149.35$ mT and $\mu_0 M_s = 316.57$ mT at 4 K by fixing $\gamma/2\pi = 28$ GHz/T. According to Eq. (3), the acoustic mode m_a is excited by the out-of-plane microwave magnetic field h_θ , and the optical mode m_o is driven by the in-plane microwave magnetic field h_ϕ . In our experimental setup, $h_\theta = h_z$ and $h_\phi = h_y \cos \phi$. The electromagnetic field in the cavity without sample can be theoretically modeled as an RLC circuit. The microwave current $j(t)$ in the cavity driven by the rf voltage satisfies Kirchhoff's equation [14].

In the hybrid system, the coupling of the antiferromagnet and cavity can be theoretically connected by Faraday induction and Ampère's law [7]. The microwave magnetic field generated by the microwave current through the cavity follows Ampère's law and drives the precession of magnons. In reverse, the precession magnons can induce an additional voltage for the RLC circuit according to Faraday's induction law. Since the acoustic mode is driven by h_θ , the voltage for the cavity is produced by $dm_{a\theta}/dt$ in the coupling of the optical mode and cavity mode [8]. When the optical mode couples with the cavity mode, the additional voltage for the cavity is induced by $dm_{o\phi}/dt$ due to the excitation microwave magnetic field for the optical mode being h_ϕ [8]. In order to confirm the contributions of the net magnetization $\mathbf{M} = \mathbf{M}_0^{\text{eq}} + \mathbf{m}$ and the Néel vector $\mathbf{N} = \mathbf{N}_0^{\text{eq}} + \mathbf{n}$ in the

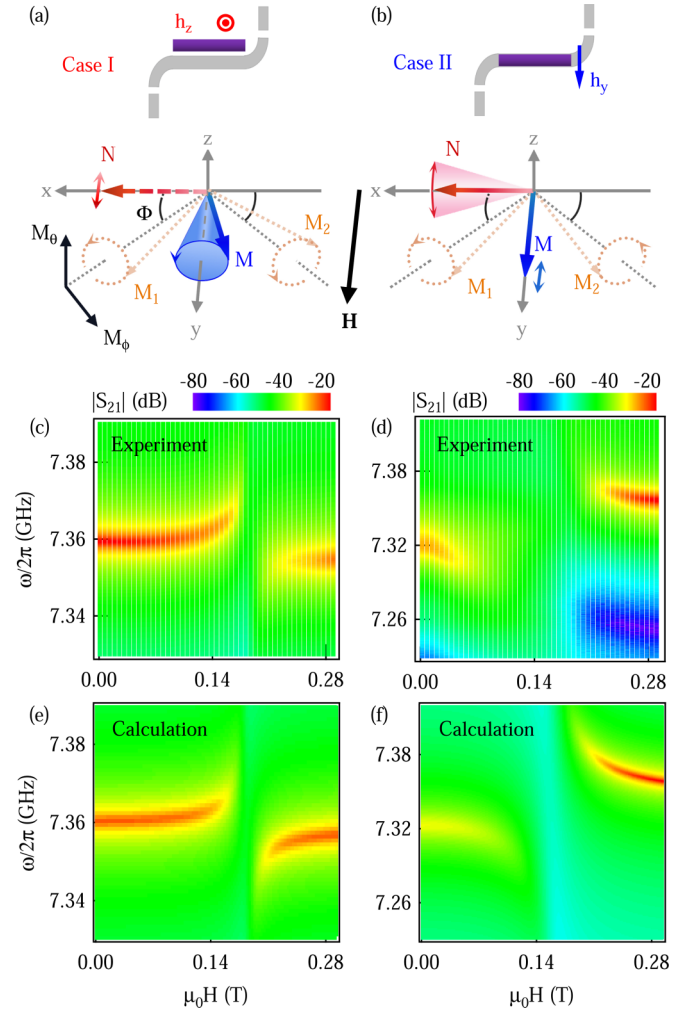


FIG. 3. Schematic diagrams of the magnetization procession for the (a) acoustic mode and (b) optical mode with the rectangular sample respectively placed on the side and on the top of the cavity. The transmission spectra mappings in the experiment for the (c) acoustic mode and (d) optical mode coupling with the cavity mode in the spin-flop transition. The corresponding theoretical results of the coupled systems for the (e) acoustic-cavity modes and (f) optical-cavity modes are calculated by Eq. (5).

coupling system, the dynamics part of the magnons in the antiferromagnetic resonances are described by \mathbf{m} and \mathbf{n} . The acoustic mode and optical mode coupling with the cavity mode can be respectively expressed by the following eigenvalue equations,

$$\Omega_a \begin{pmatrix} m_{a\theta} \\ h_\theta \end{pmatrix} = 0, \quad (4a)$$

$$\Omega_o \begin{pmatrix} \cos^2 \phi m_{o\phi} + \sin^2 \phi n_{o\phi} \\ h_\phi \end{pmatrix} = 0, \quad (4b)$$

with

$$\Omega_a \equiv \begin{pmatrix} \omega^2 - \omega_{ra}^2 - i\alpha\omega\omega_{pa} & 2\omega_m(2\omega_e \sin^2 \phi + i\alpha\omega) \\ K_a^2\omega^2 & \omega^2 - \omega_{ca}^2 - 2i\beta_a\omega_{ca}\omega \end{pmatrix},$$

$$\Omega_o \equiv \begin{pmatrix} \omega^2 - \omega_{ro}^2 - i\alpha\omega\omega_{po} & 2\omega_m \cos^2 \phi (\omega_m + i\alpha\omega) \\ K_o^2\omega^2 & \omega^2 - \omega_{co}^2 - 2i\beta_o\omega_{co}\omega \end{pmatrix},$$

where $\omega_{ca}/2\pi = 7.36$ GHz, $\beta_a = 1.07 \times 10^{-4}$, $\omega_{co}/2\pi = 7.357$ GHz, and $\beta_o = 1.05 \times 10^{-4}$ are extracted from the transmission spectra in the uncoupled regions. The parameter $K_{a(o)}$ is defined to describe the coupling strength between the acoustic (optical) mode and the cavity mode. In Eq. (4), only the out-of-plane component of net magnetization m_θ participates in the coupling of the acoustic mode and cavity mode. In Eq. (4 b), both the in-plane components of the net magnetization m_ϕ and Néel vector n_ϕ contribute to the coupling of the optical mode and cavity mode. Based on the microwave input-output formalism, the transmission spectrum S_{21} at a fix H field can be written as

$$S_{21a(o)} = \kappa_{a(o)} \frac{\omega^2(\omega^2 - \omega_{ra(o)}^2 - i\alpha\omega\omega_{pa(o)})}{\det \Omega_{a(o)}}, \quad (5)$$

where $\kappa_{a(o)} = 2\beta_{a(o)}$ is defined to describe the cavity cable impedance mismatch [7]. Since the magnetic moments in two sublattices are oriented parallel when the applied field $H > H_E$, the coupling equations are no longer suited in this condition.

IV. RESULTS AND DISCUSSION

We use a piece of CrCl_3 crystal with a lateral dimension of $0.3 \text{ mm} \times 4 \text{ mm}$ and a thickness of about $35 \mu\text{m}$. The sample width (0.3 mm) is less than the cavity signal linewidth (0.48 mm), so we can choose the microwave magnetic field h_z or h_x to excite the acoustic mode or the optical mode independently. The equilibrium directions of \mathbf{M}_1 and \mathbf{M}_2 have an angle ϕ relative to the x axis when the in-plane magnetic field \mathbf{H} is applied along the y axis, as shown by the gray dashed lines in Figs. 3(a) and 3(b). Because the acoustic mode is excited by the out-of-plane microwave magnetic field, we put the sample on the side of the cavity to make the acoustic mode couple with the cavity mode, as shown in case I. \mathbf{M}_1 and \mathbf{M}_2 rotate around their static magnetization directions in right-handed, and their precession components are in phase both on the x and z axis and out of phase by π on the y axis. In case II, the sample is on the top of the cavity, and the optical mode is excited by the in-plane microwave magnetic field to couple with the cavity mode. \mathbf{M}_1 and \mathbf{M}_2 for the optical mode are in phase along the y axis and opposed phase along the x and z axis.

Using VNA, we measure the microwave transmission spectra S_{21} of the coupling between the CrCl_3 crystal and the superconducting cavity. The transmission spectra mappings for the acoustic mode and optical mode coupling with a cavity mode are plotted in Figs. 3(c) and 3(d) as functions of frequency and external static magnetic field. The anti-crossing feature in both mappings reveals the coupling of the magnon and photon. In addition to the cavity mode, a faint antiresonance mode can be observed at a lower frequency in Fig. 3(d) and it also couples with the optical mode. Here, we focus on the coupling between the major cavity mode and antiferromagnetic resonance mode. Using Eq. (4), we fit the coupling constants $K_a = 0.028$ and $K_o = 0.036$ in the two coupled systems. In case I, the dissipation of the acoustic mode and cavity mode coupling system is dominated by the magnon decay. From the experimental results, we extract the coupling strength $g_a/2\pi = 14.49$ MHz, and the

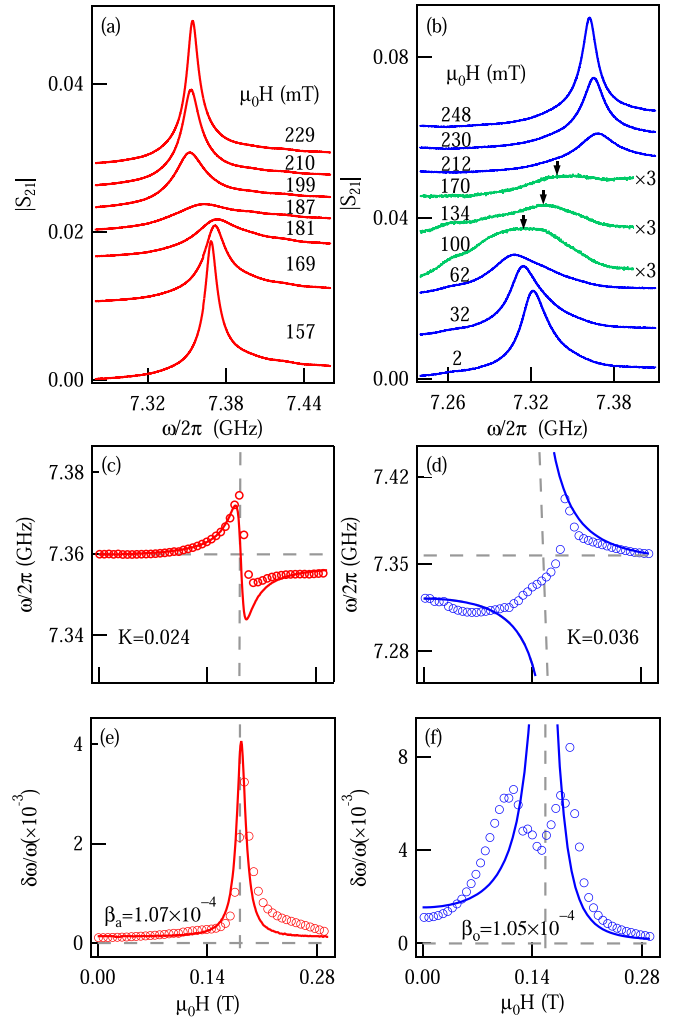


FIG. 4. Transmission spectra $|S_{21}|$ of (a) acoustic-cavity mode coupling and (b) optical-cavity mode coupling, respectively. Extracted (c) peak positions and (e) linewidth from the transmissions of the acoustic mode and cavity mode coupling system in (a). (d) Dispersion and (f) normalized linewidth of the optical-cavity modes. The solid lines in (c)–(f) correspond to the calculated results by Eq. (4).

half linewidths of the magnon $\delta\omega_{ma}/2\pi = 235.52$ MHz and photon $\delta\omega_{ca}/2\pi = 0.79$ MHz, which indicates the coupling of the acoustic mode and cavity mode falls in the Purcell regime [10]. In case II, the half linewidths of the magnon and photon are $\delta\omega_{mo}/2\pi = 235.4$ MHz and $\delta\omega_{co}/2\pi = 0.77$ MHz, respectively. Fitting by Eq. (5) with $K_o = 0.036$, we obtain the coupling strength of the optical mode and cavity mode $g_o/2\pi = 147.1$ MHz. Therefore, the coupling of the optical mode and cavity mode is also in the Purcell regime. Putting the coupling constants $K_a = 0.028$ and $K_o = 0.036$ in Eq. (5), the calculated transmission spectra mappings of the acoustic mode and optical mode coupling with the cavity modes are plotted in Figs. 3(e) and 3(f) and show the same characteristics with the experimental results.

The individual transmission spectra $|S_{21}|$ of the cavity mode coupling to the acoustic mode and the optical mode with the magnetization in the spin-flop transition are respectively plotted in Figs. 4(a) and 4(b) as functions of frequency at

different applied magnetic fields. The most important characteristics of the coupling are the shifting resonance peaks and the linewidth variations at different H fields. To further analyze the characteristics of the coupling between antiferromagnetic resonance modes and cavity modes, the resonance frequencies ω and the normalized half width $\delta\omega/\omega$ extracted from the transmission spectra are plotted in Figs. 4(c)–4(f). The classical distorted dispersions, as shown in Figs. 4(c) and 4(d), indicate the coupling between the magnon modes and cavity modes. The normalized half width, as shown in Figs. 4(e) and 4(f), quickly increases from cavity damping $\beta_{a(o)}$ to magnon damping α and vice versa. The increase of damping indicates the energy exchanges between the magnon in CrCl_3 and photon in the cavity, and the exchange efficiency achieves a maximum at the external magnetic field of the magnon mode and photon mode crossing point. The solid lines in Figs. 4(c)–4(f) are the results calculated by Eq. (5). The normalized linewidth evolution for the experimental and theoretical results in Fig. 4(e) do not match very well near the mode crossing point. These deviations are caused by the faint signal of the coupling between the antiresonance mode and optical mode, which cannot be eliminated in the measurement. Though the amplitude of the coupled mode caused by the antiresonance mode is much weaker than that caused by the cavity mode, the superposition of the faint signal results in a decrease of the normalized linewidth near the intersection of the optical mode and cavity mode.

V. CONCLUSION

In summary, we study magnon-photon coupling in an antiferromagnet with the noncollinear magnetizations configuration using a CrCl_3 crystal and a superconductive microwave cavity. Our experimental results show that the acoustic mode and optical mode can separately couple with the cavity mode under the excitation of different microwave magnetic field components, and the coupling strength for the acoustic mode is larger than that for the optical mode. Furthermore, we propose a model to describe antiferromagnetic magnon and photon coupling, and we predict the contributions of the net magnetization and the Néel vector in the coupling system. These results could help understand the coupling between the microwave photons and the magnons in an antiferromagnet.

ACKNOWLEDGMENTS

This work is supported by the National Natural Science Foundation of China (NSFC Grant No. 11774200), the

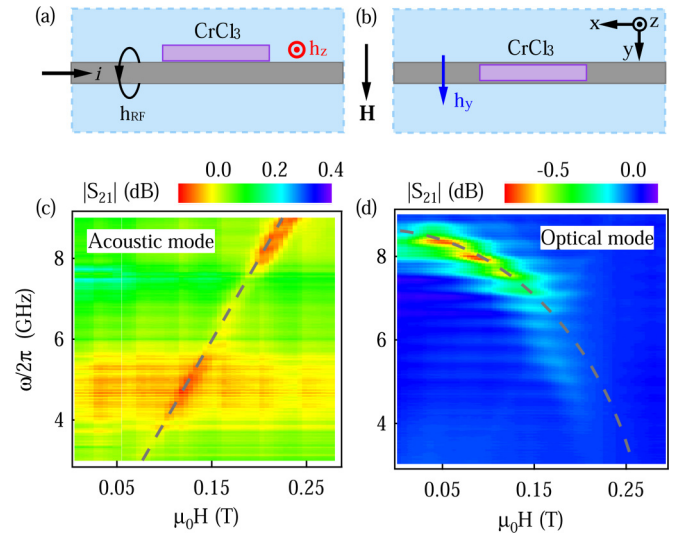


FIG. 5. Schematic diagrams used to separately measure the (a) acoustic mode and (b) optical mode, respectively. The transmission spectra mappings for the (c) acoustic mode and (d) optical mode.

Shandong Provincial Natural Science Foundation (Grant No. ZR2019JQ02), and the Youth Interdisciplinary Science and Innovative Research Groups of Shandong University.

APPENDIX: RESONANCE OF ACOUSTIC MODE AND OPTICAL MODE

To demonstrate the selective excitation of the acoustic mode and optical mode, we use VNA to measure the transmission spectra by changing the position of the CrCl_3 sample on a microstrip line as shown in Fig. 5. The microwave current flows through the line to generate the microwave magnetic field (h_y and h_z) and the static magnetic field H is applied along the y axis. When the CrCl_3 sample is placed on the side of the microstrip line as shown in Fig. 5(a), the acoustic mode can be excited by the microwave magnetic field h_z . The transmission spectra mapping for the acoustic mode, whose resonance frequency ω increases with an increase of the H field, is plotted as a function of ω and H in Fig. 5(c). When the CrCl_3 sample is loaded on the top of the microstrip line, as shown in Fig. 5(b), the magnons are driven by the microwave magnetic field h_y . Figure 5(d) shows the optical mode dispersion. The dashed lines in Figs. 5(c) and 5(d) are the fitting results.

- [1] Ö. O. Soykal and M. E. Flatté, Strong Field Interactions Between a Nanomagnet and a Photonic Cavity, *Phys. Rev. Lett.* **104**, 077202 (2010).
- [2] Y. Kubo, C. Grezes, A. Dewes, T. Umeda, J. Isoya, H. Sumiya, N. Morishita, H. Abe, S. Onoda, T. Ohshima, V. Jacques, A. Dréau, J.-F. Roch, I. Diniz, A. Auffeves, D. Vion, D. Esteve, and P. Bertet, Hybrid Quantum Circuit with a Superconducting Qubit Coupled to a Spin Ensemble, *Phys. Rev. Lett.* **107**, 220501 (2011).
- [3] X. Zhang, C.-L. Zou, N. Zhu, F. Marquardt, L. Jiang, and H. X. Tang, Magnon dark modes and gradient memory, *Nat. Commun.* **6**, 8914 (2015).
- [4] R. Hisatomi, A. Osada, Y. Tabuchi, T. Ishikawa, A. Noguchi, R. Yamazaki, K. Usami, and Y. Nakamura, Bidirectional conversion between microwave and light via ferromagnetic magnons, *Phys. Rev. B* **93**, 174427 (2016).
- [5] H. Maier-Flaig, M. Harder, S. Klingler, Z. Qiu, E. Saitoh, M. Weiler, S. Geprägs, R. Gross, S. T. B. Goennenwein, and H.

- Huebl, Tunable magnon-photon coupling in a compensating ferrimagnet from weak to strong coupling, *Appl. Phys. Lett.* **110**, 132401 (2017).
- [6] S. Klingler, H. Maier-Flaig, R. Gross, C.-M. Hu, H. Huebl, S. T. B. Goennenwein, and M. Weiler, Combined Brillouin light scattering and microwave absorption study of magnon-photon coupling in a split-ring resonator/YIG film system, *Appl. Phys. Lett.* **109**, 072402 (2016).
- [7] L. Bai, M. Harder, Y. P. Chen, X. Fan, J. Q. Xiao, and C.-M. Hu, Spin Pumping in Electrodynamically Coupled Magnon-Photon Systems, *Phys. Rev. Lett.* **114**, 227201 (2015).
- [8] L. Bai, K. Blanchette, M. Harder, Y. P. Chen, X. Fan, J. Q. Xiao, and C.-M. Hu, Control of the magnon-photon coupling, *IEEE Trans. Magn.* **52**, 1000107 (2016).
- [9] H. Huebl, C. W. Zollitsch, J. Lotze, F. Hocke, M. Greifenstein, A. Marx, R. Gross, and S. T. B. Goennenwein, High Cooperativity in Coupled Microwave Resonator Ferrimagnetic Insulator Hybrids, *Phys. Rev. Lett.* **111**, 127003 (2013).
- [10] X. Zhang, C. Zou, L. Jiang, and H. X. Tang, Strongly Coupled Magnons and Cavity Microwave Photons, *Phys. Rev. Lett.* **113**, 156401 (2014).
- [11] B. M. Yao, Y. S. Gui, Y. Xiao, H. Guo, X. S. Chen, W. Lu, C. L. Chien, and C.-M. Hu, Theory and experiment on cavity magnon-polariton in the one-dimensional configuration, *Phys. Rev. B* **92**, 184407 (2015).
- [12] N. Kostylev, M. Goryachev, and M. E. Tobar, Superstrong coupling of a microwave cavity to yttrium iron garnet magnons, *Appl. Phys. Lett.* **108**, 062402 (2016).
- [13] V. Castel, R. Jeunehomme, J. B. Youssef, N. Vukadinovic, A. Manchec, F. K. Dejene, and G. E. W. Baue, Thermal control of the magnon-photon coupling in a notch filter coupled to a yttrium iron garnet/platinum system, *Phys. Rev. B* **96**, 064407 (2017).
- [14] V. L. Grigoryan, K. Shen, and K. Xia, Synchronized spin-photon coupling in a microwave cavity, *Phys. Rev. B* **98**, 024406 (2018).
- [15] M. Harder, Y. Yang, B. M. Yao, C. H. Yu, J. W. Rao, Y. S. Gui, R. L. Stamps, and C.-M. Hu, Level Attraction Due to Dissipative Magnon-Photon Coupling, *Phys. Rev. Lett.* **121**, 137203 (2018).
- [16] Y. Li, T. Polakovic, Y. Wang, J. Xu, S. Lendinez, Z. Zhang, J. Ding, T. Khaire, H. Saglam, R. Divan, J. Pearson, W. Kwok, Z. Xiao, V. Novosad, A. Hoffmann, and W. Zhang, Strong Coupling Between Magnons and Microwave Photons in On-Chip Ferromagnet-Superconductor Thin-Film Devices, *Phys. Rev. Lett.* **123**, 107701 (2019).
- [17] J. T. Hou and L. Liu, Strong Coupling Between Microwave Photons and Nanomagnet Magnons, *Phys. Rev. Lett.* **123**, 107702 (2019).
- [18] P. F. Bongers and U. Enz, Metamagnetism of NaNiO_2 , *Solid State Commun.* **4**, 153 (1966).
- [19] T. Kampfrath, A. Sell, G. Klatt, A. Pashkin, S. Mährlein, T. Dekorsy, M. Wolf, M. Fiebig, A. Leitenstorfer, and R. Huber, Coherent terahertz control of antiferromagnetic spin waves, *Nat. Photonics* **5**, 31 (2011).
- [20] S. Baierl, J. H. Mentink, M. Hohenleutner, L. Braun, T.-M. Do, C. Lange, A. Sell, M. Fiebig, G. Woltersdorf, T. Kampfrath, and R. Huber, Terahertz-Driven Nonlinear Spin Response of Antiferromagnetic Nickel Oxide, *Phys. Rev. Lett.* **117**, 197201 (2016).
- [21] T. Moriyama, K. Hayashi, K. Yamada, M. Shima, Y. Ohya, and T. Ono, Intrinsic and extrinsic antiferromagnetic damping in NiO, *Phys. Rev. Materials* **3**, 051402(R) (2019).
- [22] T. Moriyama, K. Hayashi, K. Yamada, M. Shima, Y. Ohya, and T. Ono, Tailoring THz antiferromagnetic resonance of NiO by cation substitution, *Phys. Rev. Materials* **4**, 074402 (2020).
- [23] T. Moriyama, K. Hayashi, K. Yamada, M. Shima, Y. Ohya, Y. Tserkovnyak, and T. Ono, Enhanced antiferromagnetic resonance linewidth in NiO/Pt and NiO/Pd, *Phys. Rev. B* **101**, 060402(R) (2020).
- [24] H. Y. Yuan and X. R. Wang, Magnon-photon coupling in antiferromagnets, *Appl. Phys. Lett.* **110**, 082403 (2017).
- [25] Y. Xiao, X. H. Yan, Y. Zhang, V. L. Grigoryan, C. M. Hu, H. Guo, and K. Xia, Magnon dark mode of an antiferromagnetic insulator in a microwave cavity, *Phys. Rev. B* **99**, 094407 (2019).
- [26] M. Mergenthaler, J. Liu, J. J. Le Roy, N. Ares, A. L. Thompson, L. Bogani, F. Luis, S. J. Blundell, T. Lancaster, A. Ardavan, G. A. D. Briggs, P. J. Leek, and E. A. Laird, Strong Coupling of Microwave Photons to Antiferromagnetic Fluctuations in an Organic Magnet, *Phys. Rev. Lett.* **119**, 147701 (2017).
- [27] M. Bialek, A. Magrez, and J.-Ph. Ansermet, Spin-wave coupling to electromagnetic cavity fields in dysprosium ferrite, *Phys. Rev. B* **101**, 024405 (2020).
- [28] J. R. Everts, G. G. G. King, N. J. Lambert, S. Kocsis, S. Rogge, and J. J. Longdell, Ultrastrong coupling between a microwave resonator and antiferromagnetic resonances of rare-earth ion spins, *Phys. Rev. B* **101**, 214414 (2020).
- [29] M. A. McGuire, G. Clark, S. KC, W. M. Chance, G. E. Jellison, Jr., V. R. Cooper, X. Xu, and B. C. Sales, Magnetic behavior and spin-lattice coupling in cleavable van der Waals layered CrCl_3 crystals, *Phys. Rev. Materials* **1**, 014001 (2017).
- [30] D. MacNeill, J. T. Hou, D. R. Klein, P. Zhang, P. J.-Herrero, and L. Liu, Gigahertz Frequency Antiferromagnetic Resonance and Strong Magnon-Magnon Coupling in the Layered Crystal CrCl_3 , *Phys. Rev. Lett.* **123**, 047204 (2019).
- [31] I. S. Jacobs, Spin-flopping in MnF_2 by high magnetic fields, *J. Appl. Phys.* **32**, s61 (1961).
- [32] D. Bothner, T. Gaber, M. Kemmler, D. Koelle, R. Kleiner, S. Wünsch, and M. Siegel, Magnetic hysteresis effects in superconducting coplanar microwave resonators, *Phys. Rev. B* **86**, 014517 (2012).